Electron–phonon-driven three-dimensional metallicity in an insulating cuprate

Edoardo Baldini[a,b,1], Michael A. Sentef[c], Swagata Acharya[d], Thomas Brumme[c,e], Evgeniia Sheveleva[f], Fryderyk Lyzwa[f], Ekaterina Pomjakushina[g], Christian Bernhard[f], Mark van Schilfgaarde[d], Fabrizio Carbone[a], Angel Rubio[c,h,i,1], and Cédric Weber[d,1]

[a]Institute of Physics, Laboratory for Ultrafast Microscopy and Electron Scattering, École Polytechnique Fédérale de Lausanne, CH-1015 Lausanne, Switzerland; [b]Institute of Chemical Sciences and Engineering, Laboratory of Ultrafast Spectroscopy, École Polytechnique Fédérale de Lausanne, CH-1015 Lausanne, Switzerland; [c]Max Planck Institute for the Structure and Dynamics of Matter, D-22761 Hamburg, Germany; [d]Department of Physics, King's College London, London WC2R 2LS, United Kingdom; [e]Wilhelm Ostwald Institut of Physical and Theoretical Chemistry, University of Leipzig, D-04103 Leipzig, Germany; [f]Department of Physics, University of Fribourg, CH-1700 Fribourg, Switzerland; [g]Solid State Chemistry Group, Laboratory for Multiscale Materials Experiments, Paul Scherrer Institute, CH-5232 Villigen PSI, Switzerland; [h]Nano-Bio Spectroscopy Group, Departamento de Física de Materiales, Universidad del País Vasco, 20018 San Sebastían, Spain; and [i]Center for Computational Quantum Physics, The Flatiron Institute, New York, NY 10010

Contributed by Angel Rubio, February 11, 2020 (sent for review November 8, 2019; reviewed by Riccardo Comin and Zhi-Xun Shen)

The role of the crystal lattice for the electronic properties of cuprates and other high-temperature superconductors remains controversial despite decades of theoretical and experimental efforts. While the paradigm of strong electronic correlations suggests a purely electronic mechanism behind the insulator-to-metal transition, recently the mutual enhancement of the electron–electron and the electron–phonon interaction and its relevance to the formation of the ordered phases have also been emphasized. Here, we combine polarization-resolved ultrafast optical spectroscopy and state-of-the-art dynamical mean-field theory to show the importance of the crystal lattice in the breakdown of the correlated insulating state in an archetypal undoped cuprate. We identify signatures of electron–phonon coupling to specific fully symmetric optical modes during the buildup of a three-dimensional (3D) metallic state that follows charge photodoping. Calculations for coherently displaced crystal structures along the relevant phonon coordinates indicate that the insulating state is remarkably unstable toward metallization despite the seemingly large charge-transfer energy scale. This hitherto unobserved insulator-to-metal transition mediated by fully symmetric lattice modes can find extensive application in a plethora of correlated solids.

insulator–metal transition | cuprates | ultrafast optics | electron–phonon coupling

The insulator-to-metal transition (IMT) and high-temperature (T_C) superconductivity in cuprates are central topics in condensed-matter physics (1, 2). A crucial roadblock toward a complete understanding of the IMT and the details of the phase diagram in these compounds lies in the strong-correlation problem. Electron–electron correlations have long been thought to be the dominant actor responsible for the IMT, whereas the crystal lattice and the electron–phonon coupling have played a secondary role. As a result, much of our present knowledge about the relevant physics of cuprates has been framed around the two-dimensional (2D) Hubbard model.

Recently, this purely electronic scenario has been challenged by a body of work. On the theory side, it is believed that the selective modification of bond lengths and angles can trigger a localization–delocalization transition in the undoped parent compounds (3, 4) or even lead to a concomitant increase of the superconducting T_C (5). On the experimental side, the interplay between the electron–electron and the electron–phonon interaction has been proposed as an efficient pathway to stabilize superconductivity (6–9). The emergent picture is that electronic correlations and electron–phonon coupling cannot be considered as independent entities in the high-T_C problem, but rather as equally fundamental interactions that can mutually enhance each other.

While this intertwined character of different interactions makes cuprates excellent candidates to benchmark new theories in correlated-electron physics, it also renders these solids a puzzling case to understand (10). First-principles theoretical descriptions that deal with strong correlations are notoriously difficult to handle, and only now powerful methods are becoming available that render the problem tractable on modern computers (5, 11). At the same time, experimental progress in disentangling intricate interactions relies on the development of novel spectroscopic techniques. In particular, driving complex systems out of equilibrium and monitoring their real-time behavior with ultrafast probes (12) have evolved as a promising strategy to uncover the relevance of various microscopic degrees of freedom and the mutual forces between them (13).

The application of ultrafast methods to undoped cuprates has revealed preliminary details on the dynamics underlying the IMT. This was accomplished by photodoping particle–hole pairs in the CuO_2 planes with a short laser pulse while monitoring the change in the optical absorption spectrum with a delayed continuum probe (14, 15). The extremely fast timescale (40 to 150 fs) associated with the rise of the low-energy Drude response was

Significance

Elucidating the role of different degrees of freedom in a phase transition is crucial in the comprehension of complex materials. A phase transformation that attracts significant interest is the insulator-to-metal transition of Mott insulators, in which the electrons are thought to play the dominant role. Here, we use ultrafast laser spectroscopy and theoretical calculations to unveil that the correlated insulator La_2CuO_4, precursor to high-temperature superconductivity, is unstable toward metallization when its crystal structure is displaced along the coordinates of specific vibrational modes. This, in turn, supports the involvement of the lattice in this phase transition. Our results pave the way toward the geometrical design of metallic states in Mott insulators, with technological potential for ultrafast switching devices at room temperature.

Author contributions: E.B., M.A.S., A.R., and C.W. designed research; E.B., S.A., T.B., E.S., F.L., E.P., M.v.S., A.R., and C.W. performed research; E.B. and F.C. analyzed data; and E.B., M.A.S., C.B., A.R., and C.W. wrote the paper.

Reviewers: R.C., Massachusetts Institute of Technology; and Z.-X.S., Stanford University.

The authors declare no competing interest.

[1]To whom correspondence may be addressed. Email: angel.rubio@mpsd.mpg.de, cedric.weber@kcl.ac.uk, or ebaldini@mit.edu.

This article contains supporting information online at https://www.pnas.org/lookup/suppl/doi:10.1073/pnas.1919451117/-/DCSupplemental.

First published March 11, 2020.

found to be imprinted onto the dynamical evolution of the optical charge-transfer (CT) excitation in the visible range. Within 200 fs from its formation, the mobile charges freeze into localized midgap states owing to the concomitant action of polar lattice modes and spin fluctuations (16). Finally, the self-trapped carriers release energy in the form of heat over a picosecond timescale.

Despite their pioneering contribution, these works have left several fundamental questions unanswered. First, the use of cuprate thin films has hindered the study of the charge dynamics along the crystallographic c axis. Hence, it is unknown whether the transient metallic state has a purely 2D nature or whether it also involves a certain degree of interlayer transport. Furthermore, the high temperature employed in these experiments has masked the observation of possible bosonic collective modes that cooperate with the charge carriers to induce the IMT.

Here we combine ultrafast optical spectroscopy and first-principles calculations to unravel the intricate role of the electron–phonon coupling in the stability of the insulating state of a prototypical cuprate parent compound. By measuring the nonequilibrium response of different elements of the optical conductivity tensor, we reveal that rapid injection of particle–hole pairs in the CuO_2 planes leads to the creation of a three-dimensional (3D) metallic state that has no counterpart among the chemically doped compounds and is accompanied by a complex motion of the ionic positions along the coordinates of fully symmetric modes. The information gleaned from our experiment about the phonons that strongly couple to the mobile charges is supported by a state-of-the-art theoretical framework that unveils a striking instability of the insulating state against the displacement of the same lattice modes. These findings indicate that the light-induced IMT in cuprates cannot be interpreted as a purely electronic effect, calling for the involvement of intertwined degrees of freedom in its dynamics. More generally, these results open an avenue toward the phonon-driven control of the IMT in a wide class of insulators in which correlated electrons are strongly coupled to fully symmetric lattice modes.

Results

Crystal Structure and Equilibrium Optical Properties. As a model material system we study La_2CuO_4 (LCO), one of the simplest insulating cuprates exhibiting metallicity upon hole doping. In this solid, the 2D network of corner-sharing CuO_4 units is accompanied by two apical O atoms below and above each CuO_4 plaquette. As a result, the main building blocks of LCO are CuO_6 octahedra (Fig. 1*A*) that are elongated along the c axis due to the Jahn–Teller distortion. The unit cell of LCO is tetragonal above and orthorhombic below 560 K. A simplified scheme of the electronic density of states is shown in Fig. 1 *B*, *Left*. An energy gap (Δ_{CT}) opens between the filled O-2p band and the unoccupied Cu-3d upper Hubbard band (UHB), thus being of the CT type. In contrast, the occupied Cu-3d lower Hubbard band (LHB) lies at lower energy.

First, we present the optical properties of LCO in equilibrium. Fig. 1*C* shows the absorptive part of the optical conductivity (σ_1), measured via ellipsometry. The in-plane response (σ_{1a}, solid violet curve) is dominated by the optical CT gap at 2.20 eV (17, 18). This transition is a nonlocal resonant exciton that extends at least over two CuO_4 units. The strong coupling to the lattice degrees of freedom causes its broadened shape (18–20). As such, this optical feature can be modeled as involving the formation of an electron–polaron and a hole–polaron, coupled to each other by a short-range interaction (18, 21). At higher energy (2.50 to 3.50 eV), the in-plane spectrum results from charge excitations that couple the O-2p states to both the Cu-3d states in the UHB and the La-5d/4f states. In contrast, the out-of-plane optical conductivity (σ_{1c}) is rather featureless and its monotonic increase with energy is representative of a particle–hole continuum. This spectral dependence reflects the more insulating nature of LCO along the c axis, which stems from the large interlayer distance between neighboring CuO_2 planes. As a consequence, over an energy scale of 3.50 eV, charge excitations in equilibrium are mainly confined within each CuO_2 plane.

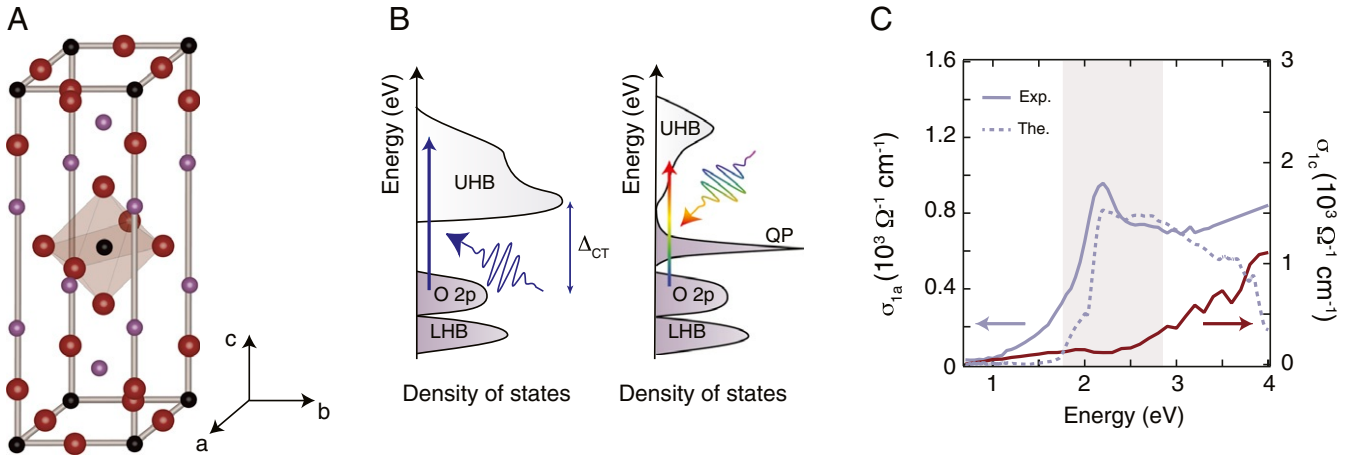

Fig. 1. (*A*) Crystallographic structure of La_2CuO_4 in its low-temperature orthorhombic unit cell. The Cu atoms are depicted in black, the O atoms in red, and the La atoms in violet. The brown shading emphasizes the CuO_6 octahedron in the center. (*B*) Schematic representation of the interacting density of states in undoped insulating (*Left*) and photodoped metallic (*Right*) La_2CuO_4. The O-2*p*, lower Hubbard band (LHB), upper Hubbard band (UHB), and quasiparticle (QP) peak are indicated. In the insulating case, the optical charge-transfer gap (Δ_{CT}) is also specified. The blue arrow indicates the 3.10-eV pump pulse, which photodopes the material and creates particle–hole pairs across the charge-transfer gap. The multicolored arrow is the broadband probe pulse, which monitors the high-energy response of the material after photoexcitation. (*C*) Real part of the optical conductivity at 10 K, measured with the electric field polarized along the *a* axis (violet solid curve) and the *c* axis (brown solid curve). The shaded area represents the spectral region monitored by the broadband probe pulse in the nonequilibrium experiment. The theory data for the in-plane response are shown as a violet dashed curve. The *a*-axis response comprises a well-defined peak in correspondence to the optical charge-transfer gap around 2.20 eV and a tail extending toward low energies down to 1.00 eV. In contrast, the *c*-axis response is featureless and increases monotonically with increasing energy, as expected from a particle–hole continuum. Exp. and The. in *C* refer to the experimental and theoretical results, respectively.

Photoinduced 3D Metallic State. We now reveal how these optical properties of LCO modify upon above-gap photoexcitation. To this aim, we tune the photon energy of an intense ultrashort laser pulse above the in-plane optical CT gap energy (blue arrow in Fig. 1 *B*, *Left*), photodoping particle–hole pairs into the CuO_2 planes. We explore an excitation regime between 0.023 and 0.075 photons per Cu atom to exceed the threshold density needed in LCO for the formation of in-plane metallic conductivity (15). We then use a continuum probe to map the pump-induced changes of the optical response over the CT energy scale (schematic in Fig. 1 *B*, *Right* and shaded area in Fig. 1*C*). Unlike previous experiments (14, 15, 22), the combination of a (100)-oriented single crystal, an accurate polarization-resolved pump–probe analysis, and low temperature allows us to identify hitherto undetected details of the light-induced IMT.

Fig. 2 *A* and *B* show the spectro-temporal evolution of the a-axis ($\Delta\sigma_{1a}$) and c-axis ($\Delta\sigma_{1c}$) differential optical conductivity in response to in-plane photoexcitation. Transient spectra at representative time delays are displayed in Fig. 2 *C* and *D*. These data are obtained from the measured transient reflectivity through a differential Lorentz analysis (23, 24), which avoids the systematic errors of Kramers–Kronig transformations on a finite energy range.

Injecting particle–hole pairs in the CuO_2 planes produces a sudden reduction in $\Delta\sigma_{1a}$ close to the optical CT excitation and to its delayed increase to positive values in the 1.80- to 2.00-eV range (Fig. 2 *A* and *C*). As explained in previous studies (14, 15), this behavior stems from the pump-induced redistribution of spectral weight from high to low energy due to several processes, among which are the ultrafast emergence of in-plane metallicity, charge localization in midgap states, and lattice heating. In particular, the latter causes the first derivative-like shape that gradually arises after several hundred femtoseconds and becomes dominant on the picosecond timescale (compare the curve at 1.50 ps in Fig. 2*C* and $\Delta\sigma_{1a}$ in *SI Appendix*, Fig. S2 *C* produced by the lattice temperature increase).

The same photodoping process also modifies $\Delta\sigma_{1c}$ (Fig. 2 *B* and *D*). At 0.10 ps, a crossover between a reduced and an increased $\Delta\sigma_{1c}$ emerges around 2.00 eV. Subsequently, the intensity weakly drops over the whole spectrum and relaxes into a negative plateau that persists for picoseconds while the system thermalizes to equilibrium. The response is featureless and one order of magnitude smaller than its in-plane counterpart. Here we show that this suppressed background is key to unraveling invaluable information on the intricate dynamics of LCO.

First, we compare the temporal evolution of $\Delta\sigma_1$ along the two crystallographic axes and focus on the dynamics close to

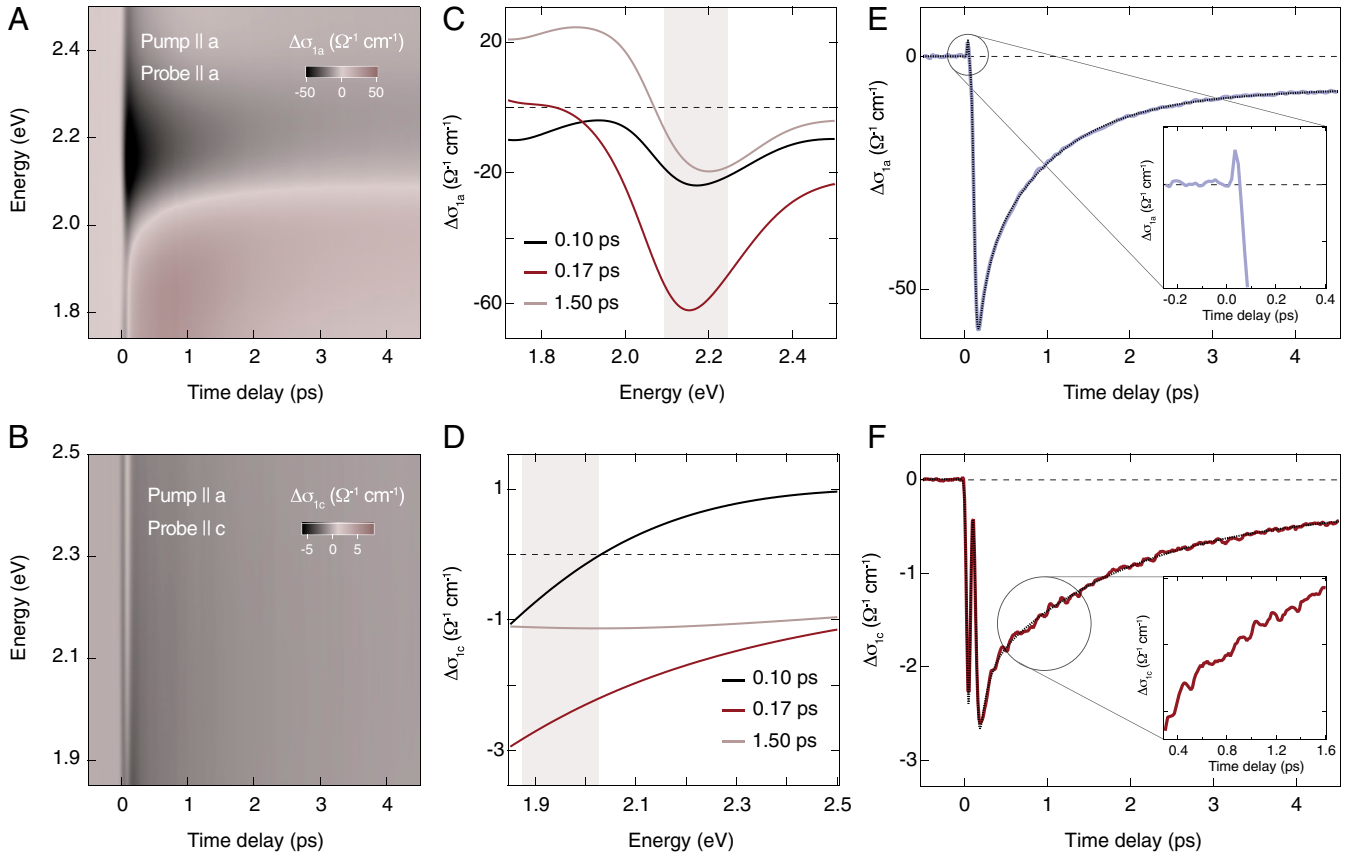

Fig. 2. (*A* and *B*) Color-coded maps of the differential optical conductivity ($\Delta\sigma_1$) at 10 K with in-plane pump polarization and (*A*) in-plane and (*B*) out-of-plane probe polarization, as a function of probe photon energy and pump–probe time delay. The pump photon energy is 3.10 eV and the excitation photon density is $x_{ph} \sim 0.06$ photons per copper atom. For in-plane probe polarization (*A*), we observe a significantly reduced $\Delta\sigma_1$ above the optical CT edge at 1.80 eV, due to spectral weight redistribution to lower energies. For out-of-plane probe polarization (*B*), the depletion in $\Delta\sigma_1$ is considerably weaker and rather featureless. Oscillatory behavior is visible in the color-coded map, hinting at coherently excited phonon modes. (*C* and *D*) Snapshots of the same data as in *A* and *B* at three different pump–probe time delays during the rise (0.10 and 0.17 ps) and the relaxation (1.50 ps) of the response. (*E* and *F*) Temporal traces of $\Delta\sigma_1$ along the *a* and *c* axes. Each temporal trace results from the integration over the energy window indicated by the shaded areas in *C* and *D*. The in-plane trace (*E*) shows a dramatic suppression and slow recovery without clearly visible coherent oscillations. A small peak emerges in the rise of the response, due to the light-induced metallic state (*E*, *Inset*). The out-of-plane trace (*F*) shows a clear signal that mimics the fast in-plane response, but relaxes with a tail exhibiting pronounced coherent oscillations (highlighted in *Inset*).

zero time delay. Fig. 2E displays a representative trace of $\Delta\sigma_{1a}$ obtained through integration around the optical CT feature. The intensity drops within ∼0.17 ps, a timescale that is significantly longer than our resolution (∼0.05 ps). The subsequent relaxation spans tens of picoseconds. A close inspection around zero time delay (Fig. 2 E, *Inset*) reveals a resolution-limited signal that emerges only partially before being buried under the pronounced intensity drop. Fig. 2F shows the out-of-plane response (integrated over the low-energy region of Fig. 2D), which shares important similarities with the in-plane signal: The intensity suppression is also complete within ∼0.17 ps and comprises a resolution-limited feature that perfectly mirrors the one along the a axis. This signal cannot originate from a leakage of the other probe polarization channel, as the shape of the $\Delta\sigma_{1c}$ spectrum has no fingerprint of the in-plane CT exciton. Furthermore, since the resolution-limited temporal response is observed only in LCO and over a broad spectral range away from the pump photon energy, it cannot be a pump-induced artifact (*SI Appendix*, section S4). Conversely, the combination of high time resolution and a continuum probe allows us to ascribe this feature to the signature imprinted onto the optical CT energy scale by a light-induced metallic state.

This conclusion naturally emerges through direct inspection of our spectro-temporal response. Previous pump–probe measurements covering the 0.10- to 2.20-eV range identified an ultrafast transfer of spectral weight from the above-gap to the below-gap region, with the establishment of Drude conductivity within the CuO_2 planes (15). Due to this spectral weight transfer, the high-energy region of the spectrum becomes sensitive to the buildup and relaxation dynamics of the itinerant carrier density. The transient metallic behavior manifests itself with a pulsed signal that modifies the optical CT gap feature and decays within 150 fs from the arrival of the pump pulse. The sign and shape of the transient metallic response depend on the nature of the optical nonlinearities induced by the delocalized carriers on the high-energy scale. In this respect, the sharp feature that we observe in our temporal traces in Fig. 2 E and F is in excellent agreement with the evolution of the in-plane Drude conductivity found in these previous experiments. More importantly, the rise of $\Delta\sigma_{1c}$ in our data closely mimics that in $\Delta\sigma_{1a}$, indicating that the metallic state has an unexpected 3D character. Quantitative information is obtained through a systematic global fit analysis of the temporal dynamics along both crystallographic axes. An accurate fit is accomplished only through a model based on that proposed in ref. 15. A Gaussian function representing the metallic state captures the fast-varying signal during the rise of the response, whereas a subsequent multiexponential relaxation comprises contributions from charge localization in midgap states and lattice heating effects. Details are given in *SI Appendix*, section S6; here we present only fits to the traces in Fig. 2 E and F, which are overlapped as dashed black lines.

Besides leaving a characteristic signature in the time domain, the 3D metallic state also influences the ultrafast spectral response of LCO. A similar behavior appears in both the absorptive and dispersive components of $\Delta\sigma_a$ and $\Delta\sigma_c$ (*SI Appendix*, Figs. S10 and S11), but with a time lag between the two directions. This suggests that the optical nonlinearities induced by the itinerant carriers onto the high-energy optical response of LCO follow distinct dynamics along the a and the c axis.

We stress that this 3D metallic state in photodoped LCO is significantly different from the case of chemically doped LCO (26). In the latter, 3D metallicity is suppressed up to doping levels as high as $p = 0.12$ (i.e., well above our photodoping density), and only in overdoped samples a well-defined Drude response is observed (27). In contrast, our findings break the scenario of an ultrafast IMT solely governed by 2D quasiparticles in the CuO_2 planes.

Dynamics of the Collective Modes. As a next step, we search for possible collective modes that strongly couple to the mobile carriers and clarify their involvement in the IMT. In this respect, we note that the lack of a significant background in $\Delta\sigma_{1c}$ uncovers a pronounced oscillatory pattern that emerges from the rise of the response and persists during its decay (Fig. 2 F, *Inset*). This coherent beating is due to collective modes displaced through the delocalized carrier density (28, 29). Similar oscillations also appear in the a-axis polarization channel (Fig. 2E), but the contrast to resolve them is lower owing to the huge relaxation background.

We assign the modes coupled to the in-plane charge density by applying a Fourier transform analysis to the original background-free transient reflectivity data to maintain high accuracy. The results, shown in Fig. 3 A and B, reveal that five bosonic excitations (labeled as $A_g(1-5)$) participate in the nonequilibrium response. Their energies match those of the five A_g phonons reported in orthorhombic LCO by spontaneous Raman scattering (25). We characterize their eigenvectors by calculating the phonon spectrum of LCO via density-functional theory (*Materials and Methods*). Fig. 3C shows the involved ionic displacements in the first half cycle of the different A_g phonons. Modes $A_g(1)$ and $A_g(2)$ exhibit staggered rotations of CuO_6 octahedra. In particular, $A_g(1)$ is the soft phonon of the orthorhombic-to-tetragonal transition. $A_g(3)$ and $A_g(4)$ present large c-axis displacements of the La atom, which in turn modify the La–apical O distance. The only difference between them lies in the displacement of the apical O: While its out-of-plane motion is the same, its in-plane motion occurs in the opposite direction. Finally, $A_g(5)$ is the breathing mode of the apical O. The Fourier transform indicates that all phonons modulate the out-of-plane response (Fig. 3B, brown curve), whereas only $A_g(1)$, $A_g(3)$, and $A_g(4)$ are unambiguously resolved in the in-plane signal (Fig. 3B, violet curve). Furthermore, since $A_g(1)$, $A_g(2)$, and $A_g(4)$ are characteristic phonons of orthorhombic LCO (25), their presence denotes that the trajectory followed by the lattice after photodoping does not evolve through the structural phase transition. Finally, no modes with symmetry other than A_g appear in our data. While this result is natural when the probe is c-axis polarized because of symmetry arguments, more noteworthy is the in-plane probe polarization case. According to Raman selection rules, modes of B_{1g} symmetry should also emerge in this polarization configuration (30). Their absence can be attributed either to the short lifetime of the B_{1g} component of the real charge-density fluctuation driving the coherent lattice response (28) or to a weak Raman cross-section in the probed spectrum.

To establish which A_g modes preferentially couple to the in-plane photodoped carriers, we also excite LCO with a light field polarized along the c axis. Despite keeping the carrier excitation density constant, this pump scheme causes a smaller drop in the transient signal amplitude and a weaker modulation depth due to the coherent lattice modes (*SI Appendix*, Fig. S7). Fourier transforming the background-free data (Fig. 3 A and B, green curves) establishes that only $A_g(1)$ and $A_g(2)$ are efficiently triggered by the out-of-plane electronic density, whereas $A_g(3)$ and $A_g(4)$ are strongly suppressed compared to the in-plane photoexcitation scheme. This suggests that periodic structural elongations and compressions of the CuO_6 octahedra along the c axis through the La atom are favorably triggered by photodoping charges within the CuO_2 planes. This aspect can be explained by noting that excitation across the optical CT gap promotes electrons in the UHB and holes in the O-2p band, thus locally removing the Jahn–Teller distortion on the CuO_6 octahedra. In the past, this picture has been explored theoretically for chemical (hole) doping, showing how the apical O approaches the Cu^{2+} ions to gain attractive electrostatic energy. Consistent with this idea, the dominant mode

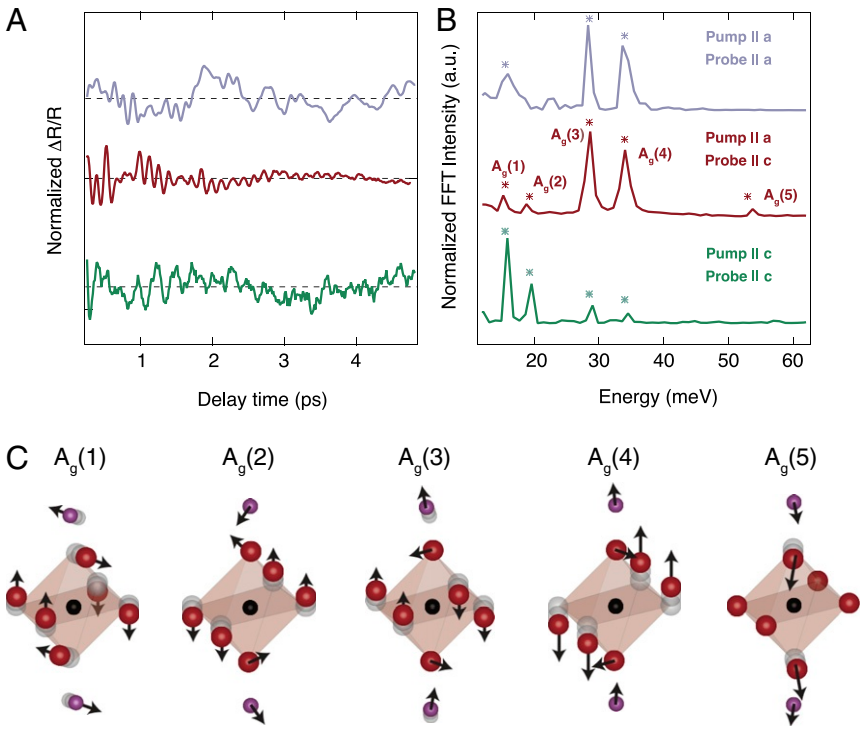

Fig. 3. (*A*) Residual reflectivity change (normalized to the largest amplitude) after subtraction of the recovering background, exhibiting coherent oscillations due to collective bosonic modes. (*B*) Fast Fourier transform of data in *A*. The data in *A* and *B* refer to different pump and probe polarizations as indicated in *B*. The traces have been selected in the probe spectral region that maximizes the oscillatory response (2.00 to 2.20 eV for the violet curve and 1.80 to 2.20 eV for the brown and the green curves). Different polarizations show the presence of a set of totally symmetric (A_g) phonon modes of the orthorhombic crystal structure. The asterisks in *B* indicate the phonon energy measured by spontaneous Raman scattering (25). a.u., arbitrary units. (*C*) Calculated eigenvectors of the five modes of A_g symmetry. Black atoms refer to Cu, red atoms to O, and violet atoms to La. Modes $A_g(1)$ and $A_g(2)$ involve staggered rotations of CuO_6 octahedra. Modes $A_g(3)$ and $A_g(4)$ present large *c*-axis displacements of the La atom, which in turn modify the La–apical O distance. The only difference between them lies in the displacement of the apical O: While its out-of-plane motion is the same, its in-plane motion occurs in the opposite direction. Mode $A_g(5)$ is the breathing mode of the apical O. The phonon spectrum has been computed using density-functional theory.

in our experiment involves coherent displacements of the apical O and the La atoms along the c axis, i.e., an oscillating motion that likely follows the destabilization of the Jahn–Teller distortion.

Role of the Electron–Phonon Coupling in the Insulator-to-Metal Transition. Our results indicate that the ultrafast 3D metallization of LCO is accompanied by a complex structural motion that is strongly coupled to the delocalized carriers. This motivates us to study theoretically whether the ionic displacements along the relevant lattice mode coordinates can also influence the electronic properties of LCO. To this end, we perform advanced calculations using dynamical mean-field theory on top of a quasiparticle self-consistent GW approach (QSGW + DMFT) (*Materials and Methods*). This recently developed method offers a nonperturbative treatment of the local spin fluctuations that are key for the electronic properties of undoped cuprates. We benchmark this technique on the in-plane equilibrium optical properties of LCO. Fig. 1C shows the calculated σ_{1a} for an undisplaced unit cell (dashed violet curve). The shape of the calculated optical spectra has a remarkable quantitative agreement with the experimental data, strongly validating our theory. Our approach accurately captures the d-p correlations that are pivotal for the Madelung energy (31), refining the description of the optical absorption spectrum of correlated insulators (32).

Using this method, we address the influence of distinct lattice modes on the electronic structure and optical properties of LCO. We compute the single-particle spectral properties and optical conductivity within the frozen-phonon approximation, i.e., by statically displacing the ions in the unit cell along the coordinates of relevant Raman-active modes. While this adiabatic method can provide information only on the electron–phonon coupling in the electronic ground state, it represents a first important step to elucidate how specific atomic motions affect the electronic properties of this correlated insulator. Fig. 4 $A-C$ shows some representative results, whereas *SI Appendix*, Figs. S13–S16 provide the full analysis. To emphasize the impact of the different ionic motions on the optical conductivity, we show spectra obtained upon displacing the unit cell of LCO by 0.04 Å along different phonon coordinates. However, smaller values of frozen lattice displacement yield similar results. Surprisingly, we observe that displacements along each of the A_g modes induce net metallization along the a axis (Fig. 4 and *SI Appendix*, Figs. S13 and S14). The system evolves into a bad metal with an incoherent quasiparticle peak in the single-particle spectral function and a broad Drude response in σ_{1a}. In contrast, modes with symmetries other than A_g cause no metallic instability within the CuO_2 planes. We also extend these calculations to the c-axis optical response and test how the out-of-plane insulating state of LCO reacts against the same lattice displacements. Capturing the correct onset of the equilibrium optical conductivity along the c axis is a very demanding computational task, as the use of electron–hole screening vertex corrections becomes crucial in the presence of very small bandwidths (33). Our current QSGW + DMFT theory level does not incorporate such vertex corrections and the resulting σ_{1c} is blueshifted compared to the experimental spectrum (*SI Appendix*, Fig. S15). Nevertheless, our approach is sufficiently robust to elucidate the effect of different ionic motions on the c-axis insulating state. The results, shown in *SI Appendix*, Fig. S16 as violet curves, confirm

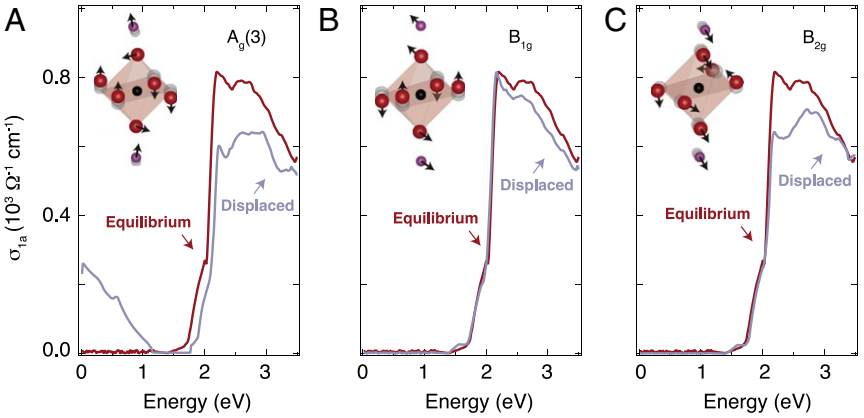

Fig. 4. (*A* − *C*) Many-body calculations of the in-plane optical conductivity for the La_2CuO_4 unit cell. Comparison between the response for the undisplaced structure (brown curve) and the response for the structure displaced by 0.04 Å along the phonon coordinates is indicated (violet curves). For displacements along totally symmetric modes (an example is shown in *A*), a metallic state emerges and gives rise to Drude spectral weight below ∼1.00 eV. In contrast, for displacements along B_g modes (examples are given in *B* and *C*), there is no metallization and hence no impact on the low-energy spectral weight inside the optical charge-transfer gap.

the trends reported for the A_g modes, establishing that displacements along their eigenvectors cause net metallization also along the c axis. These findings have three important implications: 1) The spectral region covered by our experiment is sensitive to the displacements of modes with any symmetry, ruling out the possibility of a weak Raman cross-section behind the lack of B_{1g} modes in our experiment; 2) displacements along the coordinates of modes with a fully symmetric representation can induce an IMT; and 3) the lattice-driven metallic state has a 3D nature.

Let us discuss the possible contributions that can explain the observed metallicity in the A_g-displaced structures: effective doping, change of screening, and modification of orbital overlaps. Regarding the doping into Cu-3d states, displacements along the coordinates of all Raman-active modes (except B_{3g}) lead to an increase in the hole density in the d states relative to the undisplaced case (*SI Appendix*, Table S2). In the case of the B_g modes, this effective doping yields $\sim 0.4\%$ holes for B_{1g}, $\sim 0.3\%$ holes for B_{2g}, and $\sim 1.5\%$ electrons for B_{3g}. In the case of the A_g modes (except $A_g(1)$), the hole doping reaches values larger than $\sim 3\%$. It appears that all of the Raman-active modes that cause significant effective doping in Cu-3d induce a transfer of spectral weight to lower energies, leading to weak metallization. Enhanced screening in the displaced structures could also lead to the breakdown of the insulating state via modified effective Hubbard U and CT energies. However, our estimates of the CT energy for the displaced structures show very small variation compared to that of undisplaced LCO (*SI Appendix*, Table S1). While these changes are typically larger for modes that lead to metallization, the rather small modification of the CT energy alone is unlikely to cause the loss of the insulating state. Finally, by the principle of exclusion, the orbital overlaps and thus the hopping integrals between Cu-3d and O-2p orbitals remain as the main explanation for the emerging metallic state, due to their high sensitivity to certain lattice displacements. While we do not explicitly compute values for renormalized hoppings here, the momentum-resolved spectral functions for the displaced structures (*SI Appendix*, Fig. S13) strongly suggest that modified hoppings are indeed the most important ingredient in the observed metallization.

Discussion

The fundamental and technological implications of our results are noteworthy. On the theory side, we have reported a hitherto undetected type of IMT, which applies to pure Mott/CT insulators [i.e., devoid of coexisting charge-orbital orders (34–36) and not lying in proximity to a structural transformation (37–39)]. As such, this IMT can be extended to a wide class of correlated solids (e.g., NiO, iridates, etc.). Moreover, in the specific case of cuprates, our data enrich the debate around the role and structure of the electron–phonon interaction (7, 9, 40–46). In particular, an old puzzle in the field regards the evolution of the quasiparticle-like excitations from the undoped Mott insulator to the doped compounds (19, 47). This problem is closely related to the correct identification of the chemical potential and its behavior upon hole or electron doping. A possible solution of this paradox was proposed by noting that the coherent quasiparticle scenario fails to describe the Mott insulating state and that a Franck–Condon type of broadening contributes to the lineshape of the main band in the single-particle excitation spectrum (19). In the Franck–Condon scenario, the true quasiparticle peak at half filling has a vanishingly small weight and the spectrum is dominated by incoherent sidebands due to shake-off excitations stemming from the coupling between the electrons and bosonic collective modes.

Our results add significant insights to this long-standing problem. First, the combination of our equilibrium optical data and calculations reinforces the idea that polar lattice modes cooperate with the electronic correlations to freeze quasiparticles and stabilize the insulating state of LCO (14–16, 22, 48). This is evidenced by the tail of optical spectral weight extending down to 1.00 eV in Fig. 1C, at odds with the 1.80-eV electronic-only gap retrieved by our simulations. This discrepancy can be explained by noting that our theory does not account for either the electron–phonon or the electron–hole interactions. As such, the tail emerging below 1.80 eV in σ_{1a} is most likely due to the interplay between excitonic states and polar lattice modes (49). This observation would clarify why the energy gap (and the barrier to metallicity) relevant to the transport and thermodynamic properties of insulating cuprates is much smaller that the optical CT gap (for LCO the transport gap is estimated around 0.89 eV, at the onset of the tail in σ_{1a}) (50–52). The same polar lattice modes would also be responsible for the charge–phonon coupling revealed by the previous photodoping experiments on LCO (14, 15), shaping the structure of the midinfrared absorption bands (16). On top of this, our study uncovers that (real) Raman-active lattice displacements can instead induce quasiparticle delocalization and trigger an IMT. Taken together, these results constitute additional proof for the role of the crystal lattice in

both quasiparticle dressing and stability toward metallization, indicating that the strong-correlation problem is incomplete without phonons.

On the applied side, the important upshot from our findings is that excitation of specific Raman-active modes shows huge potential for the control of the IMT in correlated insulators. In recent years, the notion of nonlinear phononics has opened an avenue toward the lattice-mediated control of electronic properties in a wide variety of doped correlated materials (53, 54). The underlying mechanism involves the resonant excitation of large-amplitude infrared-active modes, whose oscillation displaces the crystal along the coordinates of coupled Raman-active modes. Extending these studies to the insulating parent compounds by employing narrow-band terahertz fields and sum-frequency ionic Raman scattering (55, 56) will realize the mode-selective control of the IMT in the electronic ground state, paving the way to the use of correlated insulators in fast room-temperature devices. Finally, our joint experimental–theoretical effort points to rational-design strategies for quantum materials that exhibit a subtle interplay of electron–electron and electron–phonon interactions.

Materials and Methods

Data supporting this article are available from the authors upon reasonable request.

Single-Crystal Growth and Characterization. Polycrystalline LCO was prepared by a solid-state reaction. The starting materials La_2O_3 and CuO with 99.99% purity were mixed and ground. This process was followed by a heat treatment in air at 900 to 1050 °C for at least 70 h with several intermediate grindings. The phase purity of the resulting compound was checked with a conventional X-ray diffractometer. The resulting powder was hydrostatically pressed into rods (7 mm in diameter) and subsequently sintered at 1150C for 20 h. The crystal growth was carried out using an optical floating zone furnace (FZ-T-10000-H-IV-VP-PC; Crystal System Corp.) with four 300-W halogen lamps as heat sources. The growing conditions were as follows: The growth rate was 1 mm/h, the feeding and seeding rods were rotated at about 15 rpm in opposite directions to ensure the liquid's homogeneity, and an oxygen and argon mixture at 3 bar pressure was applied during the growth. The as-grown crystals were postannealed at 850 °C to release the internal stress and to adjust the oxygen content. One crystal was oriented in a Laue diffractometer, cut along a plane containing the *a* and *c* axes, and polished to optical quality. Initially, the Néel temperature was determined to be T_N = 260 K, which corresponds to a doping $\delta = 3 \times 10^{-3}$ and a hole content $p = 6 \times 10^{-3}$. For this reason, the crystal was annealed for 48 h to remove part of the excess oxygen. After the treatment, T_N increased to 307 K, which well agrees with the typical value found in purely undoped compounds.

Ellipsometry. We used spectroscopic ellipsometry to measure the complex dielectric function of the sample, covering the spectral range from 0.80 eV to 6.00 eV. The experiments were performed using a Woollam VASE ellipsometer. The LCO single crystal was mounted in a helium flow cryostat, allowing measurements from room temperature down to 10 K. The measurements were performed at $<10^{-8}$ mbar to prevent measurable ice condensation onto the sample. Anisotropy corrections were performed using standard numerical procedures.

Ultrafast Broadband Optical Spectroscopy. For the ultrafast optical experiments, we used an amplified laser system operating at a repetition rate of 3 kHz (57–59). The setup was based on a Ti:Sapphire oscillator, pumped by a continuous-wave Nd:YVO_4 laser, which emitted sub–50-fs pulses at 1.55 eV with a repetition rate of 80 MHz. The output of the oscillator seeded a cryo-cooled Ti:Sapphire amplifier, which was pumped by a Q-switched Nd:YAG laser. This laser system provided ∼45-fs pulses at 1.55 eV. One-third of the output, representing the probe beam, was sent to a motorized delay line to set a controlled delay between pump and probe. The 1.55-eV beam was focused on a 3-mm-thick CaF_2 cell using a combination of a lens with short focal distance and an iris to limit the numerical aperture of the incoming beam. The generated continuum covered the 1.77- to 2.90-eV spectral range. The probe was subsequently collimated and focused onto the sample through a pair of parabolic mirrors at a small angle from normal incidence. The remaining two-thirds of the amplifier output, representing the pump beam, were frequency doubled to 3.10 eV in a β-barium borate crystal and directed toward the sample under normal incidence. Along the pump path, a chopper with a 60-slot plate was inserted, operating at 1.5 kHz and phase-locked to the laser system. Both pump and probe were focused onto the sample on spots of dimensions 120 μm × 87 μm for the pump and 23 μm × 23 μm for the probe. The sample was mounted inside a closed-cycle cryostat, which provided a temperature-controlled environment in the range 10 to 340 K. The reflected probe was dispersed by a fiber-coupled 0.3-m spectrograph and detected on a shot-to-shot basis with a complementary metal-oxide semiconductor linear array. Before the data analysis, the transient reflectivity matrix was corrected for the group velocity dispersion of the probe. It is important to note that the probe beam dispersion was not a limiting factor for the time resolution of the setup, since it was given on the detection side by the much smaller effective pulse duration per detector pixel. As such, the time resolution for all probe photon energies was ∼50 fs.

Ab Initio Calculations. To characterize the lattice modes of LCO, we performed density-functional theory linear-response calculations as implemented in the Quantum Espresso package (60). We used norm-conserving pseudopotentials explicitly including semicore states (61) for La and Cu, the local density approximation (LDA) (62), and a plane-wave cutoff energy of 200 Ry on the kinetic energy. The charge density and dynamical matrices were calculated for the Γ point of the Brillouin zone using a 7 × 7 × 7 Γ-centered Monkhorst–Pack (63) electron-momentum grid and a Gaussian smearing of 0.002 Ry. The convergence with respect to all these parameters has been checked thoroughly. The experimental primitive unit cell (64) was relaxed prior to the phonon calculation which resulted in a slightly reduced volume (∼1%), typical for LDA calculations.

We modeled the optical data of LCO by combining the QS*GW* theory and DMFT calculations (5), as implemented in the Questaal package (65). (The Questaal code is freely available at http://www.questaal.org. Our *GW* implementation was adapted from the original ecalj package, now at https://github.com/tkotani/ecalj/.) The paramagnetic DMFT was combined with the QS*GW* via local Cu-3*d* projectors of the Kohn–Sham space to the correlated subspace. We carried out the calculations for nonmagnetic LCO in the orthorhombic phase with space group 64/Cmca (66), within the QS*GW* + DMFT approach (67). DMFT provides a nonperturbative treatment of the local spin fluctuations. We used the hybridization expansion flavor of the locally exact continuous-time quantum Monte Carlo solver (68) to solve the correlated impurity problem. Charge self-consistency on the static QSGW potential was performed on a 16 × 16 × 16 k-mesh, fully converging the charge. The GW self-energy (Σ^0), which varies with k much more slowly than the kinetic energy, was calculated on a 4 × 4 × 4 k-mesh and converged with rms change in $\Sigma^0 < 10^{-5}$ Ry. Subsequent DMFT calculations were iterated, and the dynamical self-energy converged in ∼15 to 20 iterations. The calculations for the single-particle responses were performed with 10^8 quantum Monte Carlo steps per core and the statistics were averaged over 64 cores. As a second step, we considered a small rigid displacement of the ionic positions in LCO along the phonon vector fields calculated from density-functional theory. Finally, we computed the optical conductivity for the different displaced structures. The largest amplitude of the considered shifts was 0.04 Å.

ACKNOWLEDGMENTS. We are grateful to Anthony J. Leggett, Antoine Georges, José Lorenzana, and Ferdi Aryasetiawan for insightful discussions. E.B. and F.C. acknowledge support from the National Center of Competence in Research - Molecular Ultrafast Science and Technology (NCCR-MUST). M.A.S. acknowledges support by the Deutsche Forschungsgemeinschaft (DFG) through the Emmy Noether program (SE 2558/2-1). T.B. and A.R. were supported by the European Research Council (ERC-2015-AdG694097), the Cluster of Excellence (Advanced Imaging of Matter [AIM]), Grupos Consolidados (IT1249-19), and SFB925 "Light induced dynamics and control of correlated quantum systems." The Flatiron Institute is a division of the Simons Foundation. E.S., F.L., and C.B. acknowledge funding from the Swiss National Science Foundation (SNSF) by Grant 200020-172611. For computational resources, S.A., M.v.S., and C.W. were supported by the Advanced Research Computing High End Resource (ARCHER) UK National Supercomputing Service and the UK Materials and Molecular Modeling Hub (Engineering and Physical Sciences Research Council [EPSRC] Grant EP/P020194/1); T.B. was also supported by the Max Planck Computing and Data Facility (MPCDF) Garching.

1. P. A. Lee, N. Nagaosa, X.-G. Wen, Doping a Mott insulator: Physics of high-temperature superconductivity. *Rev. Mod. Phys.* **78**, 17–85 (2006).
2. B. Keimer, S. A. Kivelson, M. R. Norman, S. Uchida, J. Zaanen, From quantum matter to high-temperature superconductivity in copper oxides. *Nature* **518**, 179–186 (2015).
3. C. Weber, C. Yee, K. Haule, G. Kotliar, Scaling of the transition temperature of hole-doped cuprate superconductors with the charge-transfer energy. *Europhys. Lett.* **100**, 37001 (2012).
4. P. Cai *et al.*, Visualizing the evolution from the Mott insulator to a charge-ordered insulator in lightly doped cuprates. *Nat. Phys.* **12**, 1047–1057 (2016).
5. S. Acharya *et al.*, Metal-insulator transition in copper oxides induced by apex displacements. *Phys. Rev. X* **8**, 021038 (2018).
6. A. S. Mishchenko, N. Nagaosa, Electron-phonon coupling and a polaron in the t-J model: From the weak to the strong coupling regime. *Phys. Rev. Lett.* **93**, 036402 (2004).
7. O. Gunnarsson, O. Rösch, Interplay between electron–phonon and Coulomb interactions in cuprates. *J. Phys. Condens. Matter* **20**, 043201 (2008).
8. S. Gerber *et al.*, Femtosecond electron-phonon lock-in by photoemission and x-ray free-electron laser. *Science* **357**, 71–75 (2017).
9. Y. He *et al.*, Rapid change of superconductivity and electron-phonon coupling through critical doping in Bi-2212. *Science* **362**, 62–65 (2018).
10. E. Fradkin, S. A. Kivelson, J. M. Tranquada, Colloquium: Theory of intertwined orders in high temperature superconductors. *Rev. Mod. Phys.* **87**, 457–482 (2015).
11. D. Golež, L. Boehnke, M. Eckstein, P. Werner, Dynamics of photodoped charge transfer insulators. *Phys. Rev. B* **100**, 041111 (2019).
12. C. Giannetti *et al.*, Ultrafast optical spectroscopy of strongly correlated materials and high-temperature superconductors: A non-equilibrium approach. *Adv. Phys.* **65**, 58–238 (2016).
13. M. Sentef *et al.*, Examining electron-boson coupling using time-resolved spectroscopy. *Phys. Rev. X* **3**, 041033 (2013).
14. H. Okamoto *et al.*, Ultrafast charge dynamics in photoexcited Nd_2CuO_4 and La_2CuO_4 cuprate compounds investigated by femtosecond absorption spectroscopy. *Phys. Rev. B* **82**, 060513 (2010).
15. H. Okamoto *et al.*, Photoinduced transition from Mott insulator to metal in the undoped cuprates Nd_2CuO_4 and La_2CuO_4. *Phys. Rev. B* **83**, 125102 (2011).
16. A. S. Mishchenko *et al.*, Charge dynamics of doped holes in high T_c cuprate superconductors: A clue from optical conductivity. *Phys. Rev. Lett.* **100**, 166401 (2008).
17. S. Uchida *et al.*, Optical spectra of $La_{2-x}Sr_xCuO_4$: Effect of carrier doping on the electronic structure of the CuO_2 plane. *Phys. Rev. B* **43**, 7942–7954 (1991).
18. J. P. Falck, A. Levy, M. A. Kastner, R. J. Birgeneau, Charge-transfer spectrum and its temperature dependence in La_2CuO_4. *Phys. Rev. Lett.* **69**, 1109–1112 (1992).
19. K. M. Shen *et al.*, Missing quasiparticles and the chemical potential puzzle in the doping evolution of the cuprate superconductors. *Phys. Rev. Lett.* **93**, 267002 (2004).
20. D. S. Ellis *et al.*, Charge-transfer exciton in La_2CuO_4 probed with resonant inelastic x-ray scattering. *Phys. Rev. B* **77**, 060501 (2008).
21. A. Mann *et al.*, Probing the electron-phonon interaction in correlated systems with coherent lattice fluctuation spectroscopy. *Phys. Rev. B* **92**, 035147 (2015).
22. F. Novelli *et al.*, Witnessing the formation and relaxation of dressed quasi-particles in a strongly correlated electron system. *Nat. Commun.* **5**, 5112 (2014).
23. F. Novelli *et al.*, Ultrafast optical spectroscopy of the lowest energy excitations in the Mott insulator compound YVO_3: Evidence for Hubbard-type excitons. *Phys. Rev. B* **86**, 165135 (2012).
24. S. Borroni *et al.*, Coherent generation of symmetry-forbidden phonons by light-induced electron-phonon interactions in magnetite. *Phys. Rev. B* **96**, 104308 (2017).
25. S. Nimori *et al.*, Electron-phonon interaction in $La_{2-x}Sr_xCuO_4$ investigated by Raman scattering. *Phys. Rev. B* **62**, 4142–4147 (2000).
26. M. Eckstein, P. Werner, Photoinduced states in a Mott insulator. *Phys. Rev. Lett.* **110**, 126401 (2013).
27. S. Uchida, K. Tamasaku, S. Tajima, c-axis optical spectra and charge dynamics in $La_{2-x}Sr_xCuO_4$. *Phys. Rev. B* **53**, 14558–14574 (1996).
28. J. J. Li, J. Chen, D. A. Reis, S. Fahy, R. Merlin, Optical probing of ultrafast electronic decay in Bi and Sb with slow phonons. *Phys. Rev. Lett.* **110**, 047401 (2013).
29. A. Mann *et al.*, Probing the coupling between a doublon excitation and the charge-density wave in TaS_2 by ultrafast optical spectroscopy. *Phys. Rev. B* **94**, 115122 (2016).
30. B. Mansart *et al.*, Coupling of a high-energy excitation to superconducting quasiparticles in a cuprate from coherent charge fluctuation spectroscopy. *Proc. Natl. Acad. Sci. U.S.A.* **110**, 4539–4544 (2013).
31. L. Hozoi, S. Nishimoto, G. Kalosakas, D. B. Bodea, S. Burdin, Nonlocal interactions in doped cuprates: Correlated motion of Zhang-Rice polarons. *Phys. Rev. B* **75**, 024517 (2007).
32. A. Comanac, L. de'Medici, M. Capone, A. J. Millis, Optical conductivity and the correlation strength of high-temperature copper-oxide superconductors. *Nat. Phys.* **4**, 287–290 (2008).
33. A. Go, A. J. Millis, Spatial correlations and the insulating phase of the high-T_c cuprates: Insights from a configuration-interaction-based solver for dynamical mean field theory. *Phys. Rev. Lett.* **114**, 016402 (2015).
34. L. Perfetti *et al.*, Time evolution of the electronic structure of 1*T*- TaS_2 through the insulator-metal transition. *Phys. Rev. Lett.* **97**, 067402 (2006).
35. S. Hellmann *et al.*, Time-domain classification of charge-density-wave insulators. *Nat. Commun.* **3**, 1069 (2012).
36. S. De Jong *et al.*, Speed limit of the insulator–metal transition in magnetite. *Nat. Mater.* **12**, 882–886 (2013).
37. A. Cavalleri, T. Dekorsy, H. H. W. Chong, J.-C. Kieffer, R. W. Schoenlein, Evidence for a structurally-driven insulator-to-metal transition in VO_2: A view from the ultrafast timescale. *Phys. Rev. B* **70**, 161102 (2004).
38. C. Kübler *et al.*, Coherent structural dynamics and electronic correlations during an ultrafast insulator-to-metal phase transition in VO_2. *Phys. Rev. Lett.* **99**, 116401 (2007).
39. V. R. Morrison *et al.*, A photoinduced metal-like phase of monoclinic VO_2 revealed by ultrafast electron diffraction. *Science* **346**, 445–448 (2014).
40. A. Lanzara *et al.*, Evidence for ubiquitous strong electron–phonon coupling in high-temperature superconductors. *Nature* **412**, 510–514 (2001).
41. F. Ronning *et al.*, Anomalous high-energy dispersion in angle-resolved photoemission spectra from the insulating cuprate $Ca_2CuO_2Cl_2$. *Phys. Rev. B* **71**, 094518 (2005).
42. J. Graf *et al.*, Universal high energy anomaly in the angle-resolved photoemission spectra of high temperature superconductors: Possible evidence of spinon and holon branches. *Phys. Rev. Lett.* **98**, 067004 (2007).
43. N. Gedik, D.-S. Yang, G. Logvenov, I. Bozovic, A. H. Zewail, Nonequilibrium phase transitions in cuprates observed by ultrafast electron crystallography. *Science* **316**, 425–429 (2007).
44. B. Moritz *et al.*, Effect of strong correlations on the high energy anomaly in hole-and electron-doped high-T_c superconductors. *New J. Phys.* **11**, 093020 (2009).
45. S. Johnston *et al.*, Systematic study of electron-phonon coupling to oxygen modes across the cuprates. *Phys. Rev. B* **82**, 064513 (2010).
46. J. D. Rameau *et al.*, Energy dissipation from a correlated system driven out of equilibrium. *Nat. Commun.* **7**, 13761 (2016).
47. N. Mannella *et al.*, Nodal quasiparticle in pseudogapped colossal magnetoresistive manganites. *Nature* **438**, 474–478 (2005).
48. O. Rösch *et al.*, Polaronic behavior of undoped high-T_c cuprate superconductors from angle-resolved photoemission spectra. *Phys. Rev. Lett.* **95**, 227002 (2005).
49. Y. Toyozawa, *Optical Processes in Solids* (Cambridge University Press, 2003).
50. S. Ono, S. Komiya, Y. Ando, Strong charge fluctuations manifested in the high-temperature Hall coefficient of high-T_c cuprates. *Phys. Rev. B* **75**, 024515 (2007).
51. T. Xiang, H. G. Luo, D. H. Lu, K. M. Shen, Z. X. Shen, Intrinsic electron and hole bands in electron-doped cuprate superconductors. *Phys. Rev. B* **79**, 014524 (2009).
52. A. S. Moskvin, True charge-transfer gap in parent insulating cuprates. *Phys. Rev. B* **84**, 075116 (2011).
53. R. Mankowsky, M. Först, A. Cavalleri, Non-equilibrium control of complex solids by nonlinear phononics. *Rep. Prog. Phys.* **79**, 064503 (2016).
54. A. Subedi, A. Cavalleri, A. Georges, Theory of nonlinear phononics for coherent light control of solids. *Phys. Rev. B* **89**, 220301 (2014).
55. S. Maehrlein, A. Paarmann, M. Wolf, T. Kampfrath, Terahertz sum-frequency excitation of a Raman-active phonon. *Phys. Rev. Lett.* **119**, 127402 (2017).
56. T. Terashige *et al.*, Doublon-holon pairing mechanism via exchange interaction in two-dimensional cuprate Mott insulators. *Sci. Adv.* **5**, eaav2187 (2019).
57. E. Baldini *et al.*, A versatile setup for ultrafast broadband optical spectroscopy of coherent collective modes in strongly correlated quantum systems. *Struct. Dyn.* **3**, 064301 (2016).
58. E. Baldini *et al.*, Clocking the onset of bilayer coherence in a high-T_C cuprate. *Phys. Rev. B* **95**, 024501 (2017).
59. E. Baldini *et al.*, Lattice-mediated magnetic order melting in $TbMnO_3$. *Phys. Rev. B* **97**, 125149 (2018).
60. P. Giannozzi *et al.*, Advanced capabilities for materials modelling with quantum ESPRESSO. *J. Phys. Condens. Matter* **29**, 465901 (2017).
61. C. L. Reis, J. M. Pacheco, J. L. Martins, First-principles norm-conserving pseudopotential with explicit incorporation of semicore states. *Phys. Rev. B* **68**, 155111 (2003).
62. J. P. Perdew, A. Zunger, Self-interaction correction to density-functional approximations for many-electron systems. *Phys. Rev. B* **23**, 5048–5079 (1981).
63. H. J. Monkhorst, J. D. Pack, Special points for Brillouin-zone integrations. *Phys. Rev. B* **13**, 5188–5192 (1976).
64. H. Takahashi *et al.*, Structural effects of hydrostatic pressure in orthorhombic $La_{2-x}Sr_xCuO_4$. *Phys. Rev. B* **50**, 3221–3229 (1994).
65. D. Pashov *et al.*, Questaal: A package of electronic structure methods based on the linear muffin-tin orbital technique. *Comput. Phys. Commun.* **249**, 107065 (2019).
66. M. Reehuis *et al.*, Crystal structure and high-field magnetism of La_2CuO_4. *Phys. Rev. B* **73**, 144513 (2006).
67. S. Acharya *et al.*, Evening out the spin and charge parity to increase T_C in Sr_2RuO_4. *Commun. Phys.* **2**, 163 (2019).
68. K. Haule, Quantum Monte Carlo impurity solver for cluster dynamical mean-field theory and electronic structure calculations with adjustable cluster base. *Phys. Rev. B* **75**, 155113 (2007).